NAS Technical Report
NAS-06-005
June 2006

Capsule Abort Recontact Simulation

Shishir Pandya*, Jeffrey Onufer†, William Chan‡, Goetz Klopfer§
NASA Ames Research Center, Moffett Field, CA, 94035

A study is performed to ascertain the validity of the use of inviscid and viscous simulation methods to predict the axial and normal forces during a launch abort scenario for manned space flight vehicles. The proximity drag character of the Apollo launch escape vehicle (LEV) was studied in detail in a wind tunnel during the Apollo program. Simulation results obtained during the present effort are compared to the Apollo era wind tunnel experiments. The validated simulation techniques are applied to assess the possibility of recontact between the crew capsule and the service module after a launch abort is initiated. The natural extension of the method is to assess the risk associated with the new Crew Launch Vehicle's escape system.

Nomenclature

C_p	=	Pressure coefficient
C_A	=	Axial-force coefficient
C_N	=	Normal-force coefficient
C_{Aj}	=	Thrust coefficient
α	=	Angle of attack
d	=	Service Module diameter
x	=	Longitudinal distance from apex; positive rearward
l	=	Length of the command module measured from the apex
Δx	=	Longitudinal displacement
Δz	=	Lateral displacement
$\Delta\alpha_s$	=	Relative angle between command module and service module

I. Introduction

As NASA approaches the end of the Space Shuttle era, a new era of space exploration with an Apollo-type launch system is on the horizon. The proposed Crew Launch Vehicle (CLV) is a design that combines elements of the Saturn V vehicle used during the Apollo program with some of the components used in the Space Shuttle. The new vehicle's first stage is the Space Shuttle's Solid Rocket Booster (SRB). The second stage utilizes a LH2/LOX stage that uses a derivative of the Saturn rocket's J2 engine. Atop the liquid stage is a service module (SM) and a capsule, which holds the astronauts similar to the Apollo program. The capsule and the SM together are called the Crew Exploration Vehicle (CEV). As in the Apollo program, a launch escape system consisting of the capsule connected to an escape rocket motor is used in case an abort is deemed necessary due to a failure in the launch system (Ref. 1, 2).

The abort scenario was a topic of study during the Apollo mission due to its importance as the only method of saving the astronauts in case of a disaster. During the design phase, the escape motor was sized based on astronaut safety considerations. However, during the testing phase, the Little Joe II rocket was used to perform an abort test. During this abort test, the capsule recontacted the booster shortly after abort initiation (ref. 15). This behavior is due to large changes in drag when bodies are in close proximity. Thus the effects of separation position and relative angle on the body forces are important. The primary tools available to the Apollo engineers to study these issues were analytical or empirical methods (Ref. 3), wind tunnel experiments (Refs. 4, 5) and flight tests. Since the time of the Apollo program, computer-based simulation capabilities have evolved sufficiently to play a significant role in the design and development of the CLV and for the assessment of the risks involved in the launch and abort processes.

---

* Aerospace engineer, AIAA Member.
† Computer engineer.
‡ Computer scientist, AIAA senior Member.
§ Aerospace engineer.

In order to use simulation technology for risk evaluation of a specific design, the simulation tools must be validated. This paper represents an effort to validate some of NASA's in-house capabilities to model the aerodynamics of an abort scenario. Wind tunnel data for the Apollo launch escape system is available (Ref. 4) and is used as a benchmark for simulation validation focused on the behavior of the escape system. Specifically, the axial and normal forces on the launch escape vehicle (LEV) are compared to the wind tunnel data. During the abort process, the LEV is in close proximity of the service module (SM), thus the parameters of interest are position and orientation of the LEV with respect to the SM. As a follow up to the validation study, the present capability for computing time-dependent, moving-body flow simulation is also assessed.

For inviscid simulations, the Cart3D package is used (Ref. 6). Cart3D is a component-based system that allows triangulations of separate components to be used as a starting point for a full 3D simulation of inviscid flow using telescoping Cartesian grids. In order to assess the differences between inviscid and viscous simulations, the OVERFLOW-2 code is used (ref. 7). OVERFLOW-2 is a Reynolds averaged Navier-Stokes (RANS) simulation code that uses overset mesh technology for complex geometry handling and viscous flow solution.

Steady state solutions from these two codes are compared at various free-stream conditions corresponding to the experiments in Ref. 4. The simulations from both codes are compared to the experiments to assess their usefulness for the abort scenario analysis. Finally, the unsteady, moving-body capability in the two codes is exercised to compute the time-dependent flow fields and the resulting trajectories with a comparison of the two simulations.

II. Wind tunnel experiments

Wind tunnel experiments were conducted during the Apollo program to assess the flow field interference characteristics of the Apollo launch escape system (LES). Reference 4 contains the details of these experiments. Specifically, Ref. 4 contains an investigation of the forces on the LEV as a function of the separation distance, vertical offset, and relative angle between the LEV and the SM.

The experiments were conducted in the NASA Langley 16-foot transonic wind tunnel. This tunnel has an octagonal slotted test section and speed range from M=0.3 to M=1.3. A 0.085 scale model of the LEV was tested at Mach numbers of 0.9 and 1.1.

The model of the LEV was fitted with a mechanism that used hydrogen peroxide to model the thrust and plume effects of the escape motor in the wind tunnel. Data were collected for both thrust on and off conditions. The thrust coefficient C_{Aj} as defined in Ref. 4 is used in this paper to quantify the thrust level.

A. Configuration

Figure 1 shows the configuration of the wind tunnel experiments. The LEV consists of the escape motor, the support tower, and the capsule. The motor has 4 nozzles canted 35° from the centerline. The two yaw nozzles output the same amount of thrust, while the top pitch nozzle has a smaller throat than the bottom pitch nozzle. The differential thrust is intended to pull the vehicle away from the path of the booster. The entire LEV assembly is mounted on a sting. A second, thicker sting surrounds the LEV sting and is used to mount the SM. The SM position was varied along the centerline (Δx), and perpendicular to the centerline (Δz). The angle of the SM to the LEV centerline ($\Delta\alpha_s$) is also varied.

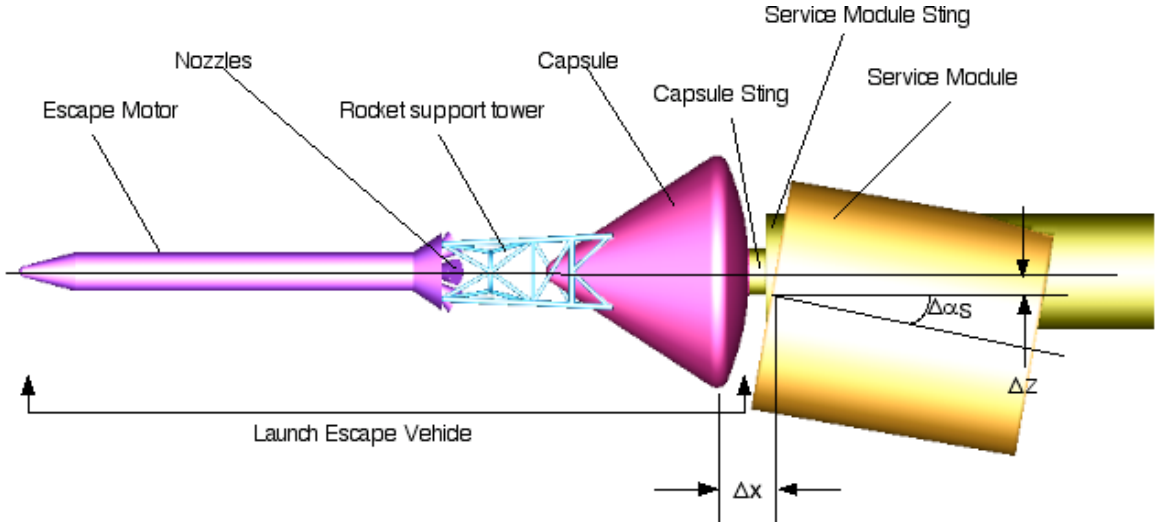


Figure 1. Geometry of the wind tunnel model

III. Simulations Methodology

Two simulation packages are used to compute solutions of the LEV in the vicinity of the SM. The Cart3D package (Ref. 6) is used to simulate the inviscid behavior of the airflow during ascent and abort of the Apollo vehicle, while Overflow (Ref. 7) is used for viscous simulations. Each step of the simulation process (geometry definition, mesh generation, flow solution) is described in the following sections.

B. Geometry definition

Chimera Grid Tools (CGT) is a collection of software written specifically for the generation and manipulation of overset surface and volume meshes (Ref. 8). The functions available in CGT allow the user to import existing geometries or generate geometries from analytical shapes. Each component of the wind tunnel model, including the structure of the support tower with its 32 struts and one ring, is made using this capability. Furthermore, CGT provides scripting so that the geometry creation can be automated, making it simpler to modify the geometry for varying SM locations and orientations.

The geometry of the Saturn V components is defined in several publications. The tower geometry is discussed in Ref. 5. In Ref. 9, the LEV is described in detail. The escape motor nozzle sizes are taken from Ref. 4 as it is important to match the wind tunnel nozzle sizes rather than the flight nozzles for comparison to the wind tunnel data. Finally, most other details of the Apollo vehicle geometry are described in Ref. 10.

C. Mesh generation

A surface mesh for each of the components is generated during the geometry definition phase. For Cart3D simulations, each component is first created with a quadrilateral mesh, which is then divided into triangles. Each component triangulation is carefully made to ensure that that the component's wetted surface forms a closed body. These triangulations are then intersected with each other to obtain the final configuration. The result is a triangulation of the vehicle with tagged components. The final triangulation is used to generate an unstructured, telescoping Cartesian mesh that is coarse in the far-field, but fine close to the surface of the vehicle (Ref. 6). The LEV model generated in this manner is shown in Figure 2 along with a cut of the Cartesian volume mesh.

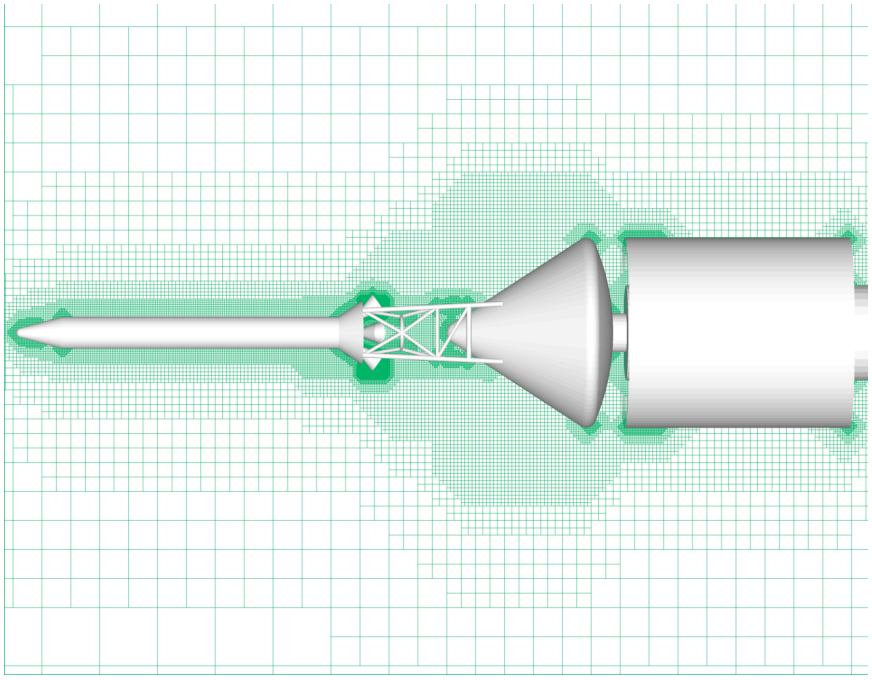


Figure 2. Geometry and Cartesian mesh around the LEV and booster

For the viscous simulations, the overset mesh approach is used. In this approach, a set of body-conforming meshes cover the near-body region, while a set of telescoping Cartesian meshes cover the off-body region. The CGT scripting capability is employed to generate the geometry, as well as an overset structured quadrilateral surface mesh(Ref. 8). The surface mesh is then used with the hyperbolic grid generation capability in CGT to create the near-body volume meshes. The off-body meshes are generated within the flow solver (Overflow-2). An example mesh around the wind tunnel geometry is shown in Figure 3.

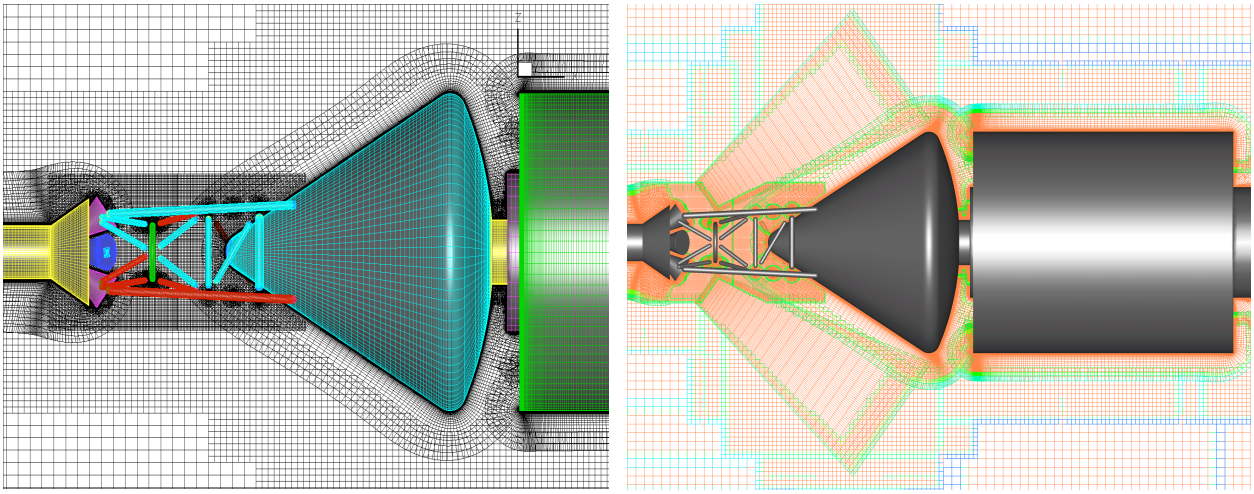


Figure 3. Geometry and overset mesh for wind tunnel geometry

D. Flow solution

The Cart3D (Ref. 6) fluid dynamics simulation software package is used to solve the Euler equations to predict inviscid fluid flow behavior. The time-dependent, moving-body capability of the Cart3D package includes body movement with 6-DOF dynamics (Ref. 11, 12). This capability is used for the dynamic abort scenario computations. Cart3D is an upwind code that uses Runge-Kutta time integration and multi-grid for convergence acceleration. The only dissipation control provided is via the limiters. Thus, a preliminary study is undertaken to to determine the multi-grid strategy and the appropriate limiter. During this study it is found that substantial flow unsteadiness develops due to the flow separation from the escape motor skirt at the capsule's maximum diameter region (shoulder), and the rear part of the SM (see Fig. 4). This unsteadiness hinders convergence and worsens with increasing angle of attack. Two levels of multi-grid and the van Leer limiter are used along with first order treatment of the cut-cells next to the vehicle surface. Running with the more dissipative min-mod limiter results in an increase of 6% in the axial-force coefficient. A mesh refinement study is also performed to gain an understanding of the solution with respect to reduction in mesh size. Table 1 shows the results of the mesh refinement with the refinement set to 12 levels and 2 additional levels of refinement for all components but the sting. It is found that the coarse mesh did not predict the value of the axial force accurately. The fine mesh resolves the unsteady features of the flow and thus encourages flow unsteadiness, resulting in lack of convergence. As a result, the medium mesh is used for the computations reported in this paper.

Table I. Mesh refinement study for the inviscid simulations, M=0.9, α*=0,* Δx=0.2, Δz=0, $\Delta\alpha_s$=0

Mesh	Starting box	Number of Grid points	C_A	C_A-experiment
Coarse	3 x 3 x 3	2 Million	0.91	1.3
Medium	5 x 5 x 5	3.7 Million	1.04	
Fine	7 x 7 x 7	8 Million	0.64(unsteady)	

In contrast to the inviscid results the Overflow-2 results all yielded steady flow fields if the appropriate procedures were followed. The grids are generated following the best practices recommended in Ref. 14. The wall-normal spacing is such that $y^+<1$ everywhere and a double fringe overlap is used. The turbulence model used is the Spalart-Allmaras model and 2nd order accurate central differences with matrix dissipation are employed for the spatial terms. It is found that the full cross-terms of the RANS are requred to obtain steady flow as the thin-layer approximation yielded unsteady flows.

As Cart3D is an inviscid simulation package, the change in forces due to viscous effects needs to be assessed. This is especially important to capture the size and extent of the regions of separated fluid. The Overflow-2 code is

used to obtain viscous simulation results and to assess if a viscous correction can be applied to the inviscid solution algorithm. Such a correction can be obtained with a few viscous data points. The moving-body capability in Overflow-2 is also employed to assess the proximity drag character during the dynamic process of abort.

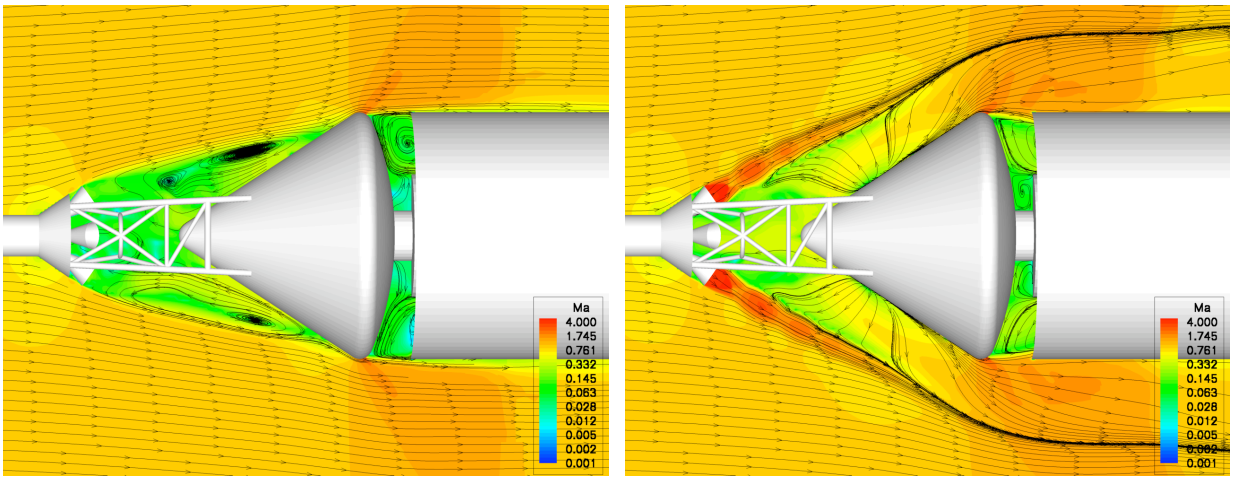


Figure 4a. Inviscid solutions with and without thrust, Mach number and streamlines, $\Delta x/d=0.2$, $\Delta z=0$, $\Delta\alpha_s=0$

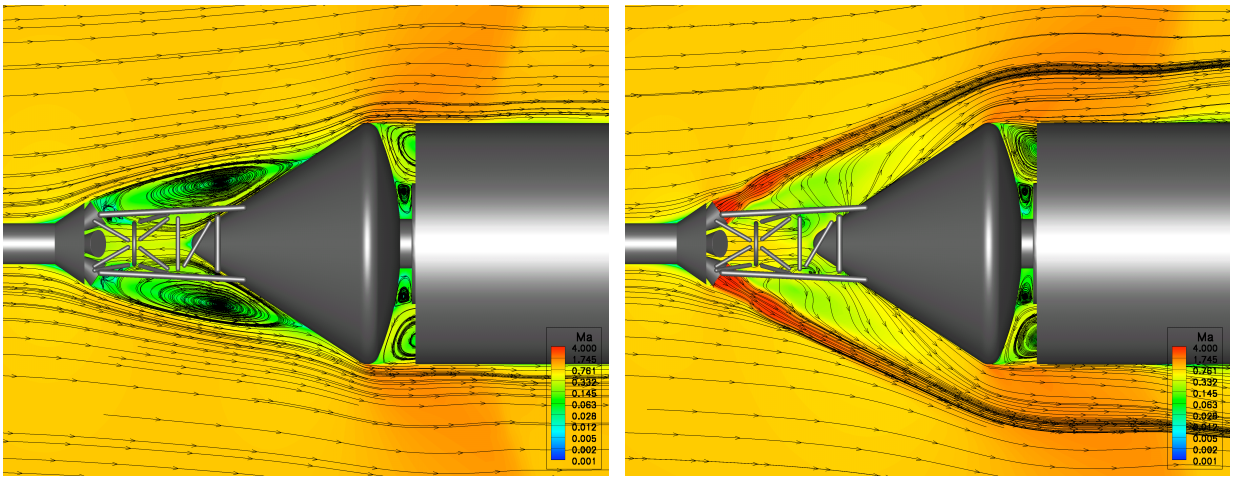


Figure 4b. Viscous solutions with and without thrust, Mach number and streamlines, $\Delta x/d=0.2$, $\Delta z=0$, $\Delta\alpha_s=0°$

E. Dynamic abort simulation

The static simulation results are compared with wind tunnel measurements to validate the simulation process. However, the goal of the simulation capability is to be able to compute flow field values during the abort sequence, which is a time-dependent maneuver with the LEV in relative motion to the booster. In order to perform the time-dependent simulation, a trajectory is assumed for the booster. The assumption made is that since the booster engines are shut-down at the time of abort, the booster continues on its original path and speed. This conservative assumption does not account for deceleration due to drag. However, it is deemed to be adequate for the present simulation.

Full 6 degrees-of-freedom dynamics are used to obtain accurate trajectories for the LEV. At every time step, the flow solver computes the flow field and the resultant forces and moments on the LEV, which are integrated by the 6-DOF dynamics package using the mass and inertial properties of the vehicle. The mass and inertial properties were obtained from Ref. 13. The dynamics module returns the new velocities and rotation rates which are used to compute the new position and orientation of the vehicle based on the user supplied time step. The vehicle is then moved that distance, orientation is changed, and the meshes are adjusted for the new position. The time-dependent metrics are computed for the moving-body/moving-grid scenario to preserve the accuracy of the flow-solver. The flow field for the next time step is computed accounting for the new positions and grid speeds. The time-dependent flow field and the trajectory of the vehicle are the results of this time-dependent solution.

IV. Results

Inviscid and viscous simulation results are compared to wind tunnel experiments (Ref. 4) to validate the computational methods. Pressures along the surface of the capsule and the SM, and axial and normal forces on the bodies are compared to wind tunnel experiments. Cases with thrust on and off at two Mach numbers and several angles of attack are evaluated.

Time-dependent simulations of the abort scenario are performed to assess the possibility of recontact. The nominal thrust and a reduced thrust scenario are simulated along with a viscous drag correction in the inviscid simulation of the reduced thrust case. The resulting trajectories are presented along with an assessment of the possibility of recontact.

A. Surface pressure

The wind tunnel experiments were primarily concerned with obtaining the aerodynamic forces (particularly axial force) on the LEV and the SM. However, pressure taps were put on the capsule and the SM. This pressure data is available in Ref. 4. A comparison of the surface pressure for the case without thrust is presented in Figure 5 for along the body of the Capsule and SM for various values of the separation distance between the LEV and SM, Δx. The computed inviscid results are lines, while the experimental results are symbols of matching color. The pressure computed in the simulations along the windward side of the capsule and on the SM compare well with experiment. The predicted base pressures on the capsule do not agree with the experiments due to lack of viscous effects in the simulation. While the inviscid flow simulation does show separated flow in the base region due to artificial dissipation (see Fig. 4), the lack of viscosity results in a faulty prediction of the separation location and size. Thus inviscid computations predict inaccurate flow in the base region.

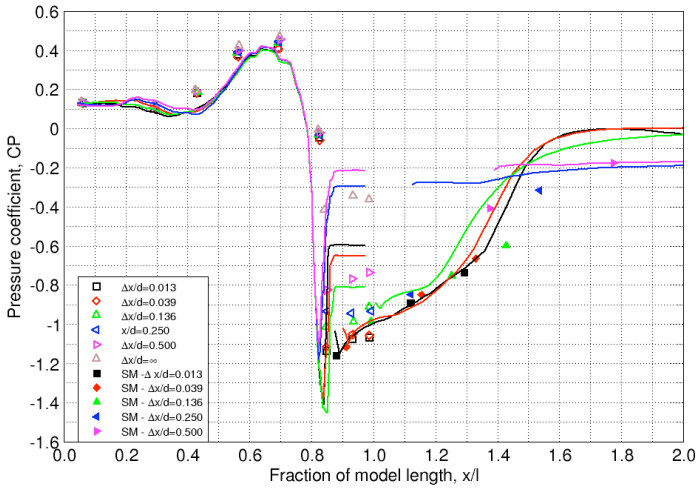


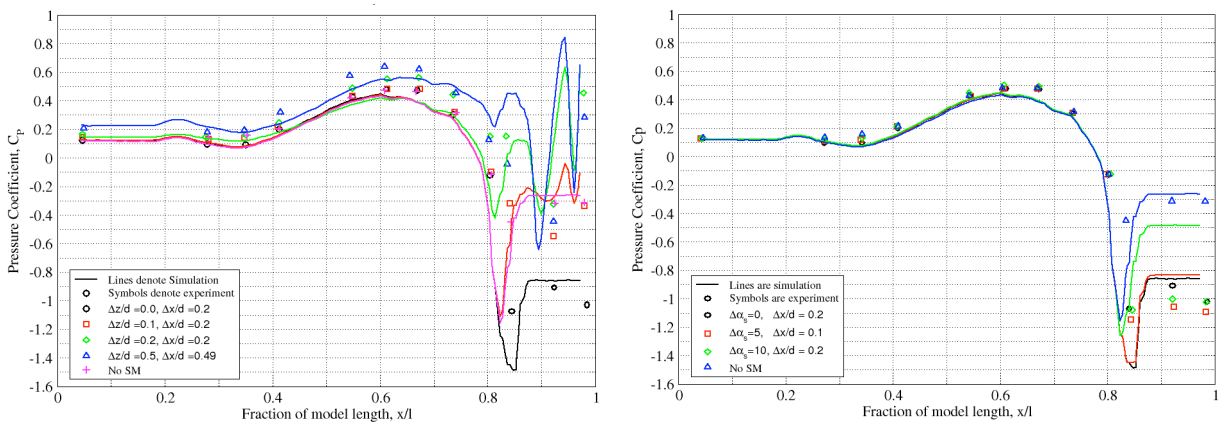
Figure 5. Pressure comparison along the body of Capsule and SM for various values of Δx at M=0.9, Δz=0, $\Delta\alpha_s$=0°, α=0° (Symbols are experiment, Lines are inviscid computation)

A second surface pressure comparison is shown in Fig. 6a with respect to the variation of SM lateral displacement, Δz. A similar pattern is observed with proper pressures obtained on the windward side of the capsule and inaccurate pressure prediction in the base region.

The third variation considered in the wind tunnel was the angle of the SM with respect to the LEV ($\Delta\alpha_s$). Shown in Figure 6b this comparison also exhibits the behavior similar to the previous pressure comparisons.

Finally, the coefficient of pressure is compared with experiments to validate the viscous method. Figure 7 shows C_p for a Δx/d of 0.2 with and without thrust. For the no-thrust case, the viscous results from the Overflow-2 code exhibit better agreement with the experiment. While the base region is not precise, it is in reasonable agreement with the average pressure value in contrast to the inviscid results in the previous figures. With thrust, the trends still match, though the pressure is over-predicted near the very front of the capsule. This region is in the separated flow behind the skirt of the escape motor. Thus, the pressures in this region are expected to vary with turbulence models. The pressure values may also be sensitive to the perfect gas assumption as we used hot air as a model for the hydrogen peroxide.

Flow-field streamline traces and Mach number contours are compared for both inviscid and viscous simulations for thrust on and off in Fig. 4. The Mach number contours are on an exponential scale and are qualitatively similar. The streamlines are surprisingly similar.



(a) variable Δz/d, $\Delta\alpha_s$ =0° *(b) variable* $\Delta\alpha_s$, Δz/d=0

Figure 6. Pressure coefficient for varying Δz *and* $\Delta\alpha_s$ respectively, *CAj=0,* α=0° *inviscid simulation*

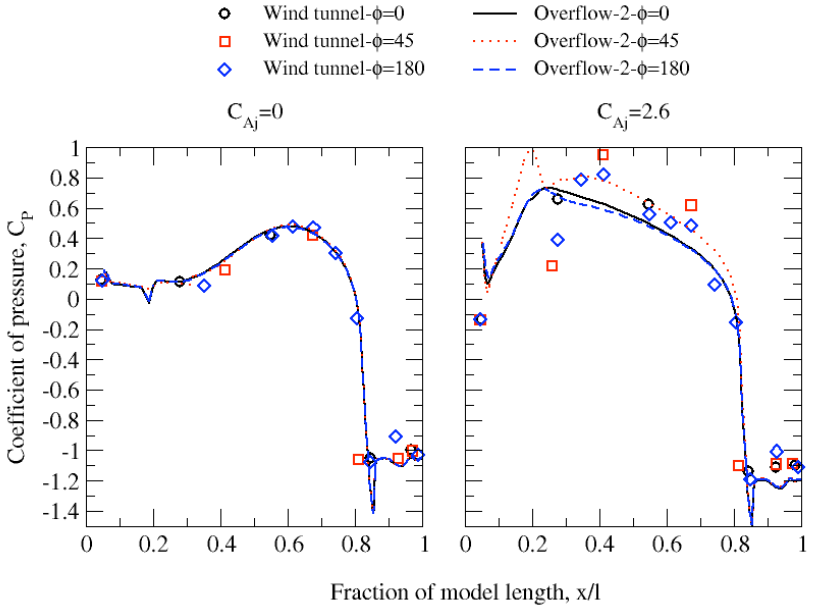


Figure 7. Pressure coefficient with and without thrust, M=0.9, Δx/d=0.2, Δz=0, $\Delta\alpha_s$=0°, α=0°, *viscous simulation*

B. Axial and normal forces

The axial and normal force coefficients are measured and reported in Ref. 4. Presented below are comparisons of these forces from simulation with wind tunnel measurements for several sets of conditions. A range of SM locations and angle orientations are simulated and their axial forces are compared. As shown in Figure 1, Δx refers to the separation distance between the SM and the capsule along the centerline and Δz refers to the vertical location of the SM with respect to the centerline. In both cases, the maximum diameter of the capsule, d, is used as a reference length. The angle $\Delta\alpha_s$ is used to denote the angle of the SM with respect to the centerline. The angle of attack is denoted by α per traditional convention and C_{Aj} is the axial-force coefficient of thrust for the escape motor and is defined in Ref. 4. C_{Aj}*=0* denotes no thrust from the escape motor and non-zero values denote a thrust setting used in the wind tunnel experiments. In the present paper, computed solutions of the cases with thrust are obtained using C_{Aj}=2.6.

Figures 8a and 8b show the comparison between inviscid simulation results and the experiments for several angles of attack. The inviscid results in Fig. 8a agree in trend with the experiments, but axial force is under-predicted. This is a due to the inability of the Euler solver to resolve the separated flow in the capsule base region as

seen in the previous section. Axial-force values computed with viscous solutions are in excellent agreement with the experimental data as seen in Fig 8a.

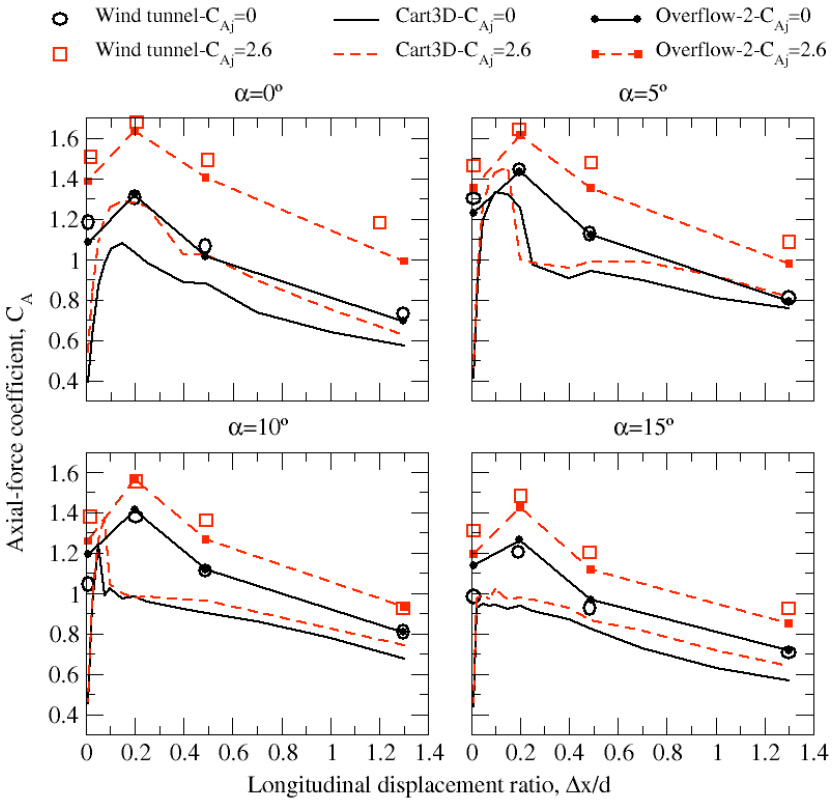


Figure 8a. Thrust and angle of attack effect on axial-force coefficient with respect to Δx, *M=0.9,* Δz/d=*0,* $\Delta\alpha_s$*=0°*

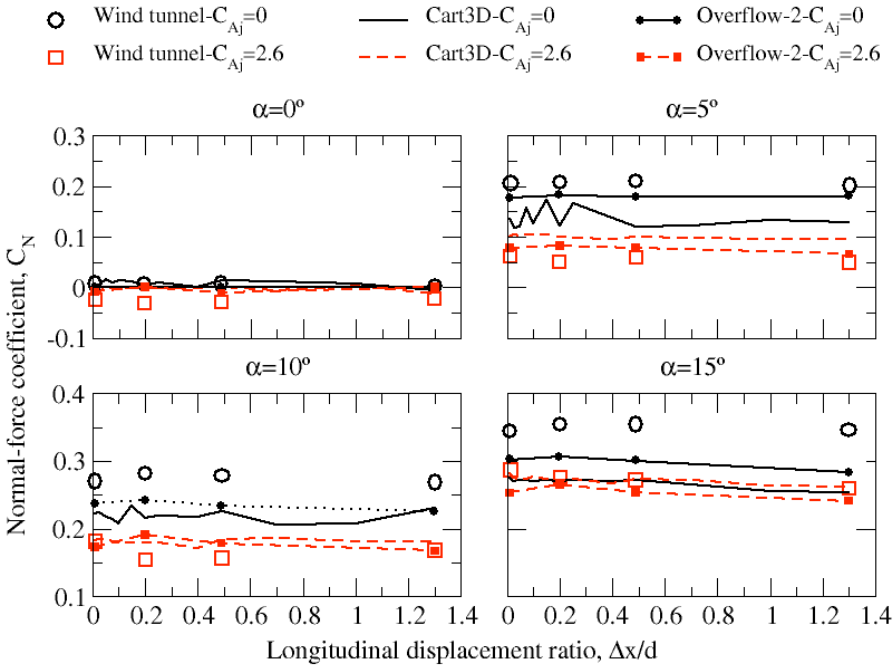


Figure 8b. Thrust and angle of attack effect on normal-force coefficient with respect to Δx, *M=0.9, Δz/d=0,* $\Delta\alpha_s$*=0°*

The experimental results show that the axial force rises between Δx=0 and Δx=0.2 (see Fig. 8a). This drag rise is not captured well by inviscid flow computations at angle of attack. Due to larger flow separation regions at angles of attack, unsteadiness plays a large role in these computations and steady state, inviscid simulations are not adequate. Normal-force coefficient is also compared to experimental results in Fig. 8b. Inviscid results once again predict a good trend, but predict a slightly low normal force. Viscous results are in good agreement with inviscid results in most cases with values that are somewhat closer to the experiment for some conditions.

Figure 9a shows inviscid and viscous simulation results for two angles of attack with and without thrust for a case where the SM is offset vertically downward (Δz/d=0.2). Once again, the trends are captured in the inviscid results, but the axial as well as normal force are under-predicted. However, the inviscid and viscous prediction of normal-force is in good agreement. Figure 9b compares the axial and normal-force coefficients for a case where the SM is tilted 10° with respect to the centerline. Once again two angles of attack are simulated for both thrust on and off conditions. The trends are good for the α=0° case. However, due to the large separation regions behind the capsule and SM, the trends do not compare well at α=10°.

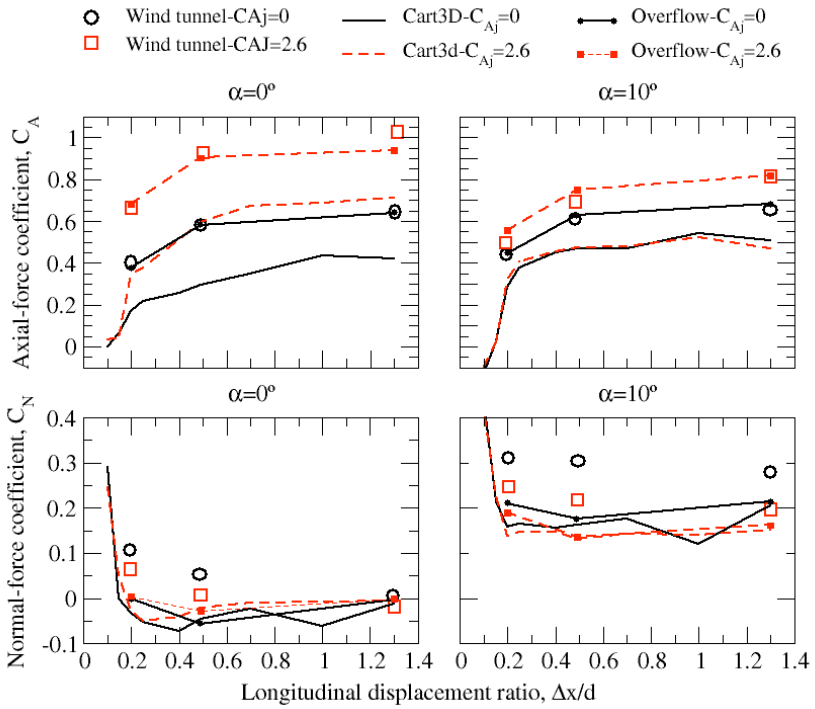


Figure 9a. Thrust and angle of attack effect on axial and normal-force coefficient with respect to Δx, *M=0.9,* Δz/d*=0.2,* $\Delta\alpha_s$*=0°*

To verify that the trends hold at α=0°, several positions and orientations of the SM are computed and compared to the experiments. These are presented in Figs. 10a and 10b. The trends indeed hold, though they are less certain when the SM is blocking a larger part of the flow and thus generating less accurate separation regions. Figure 10a also contains viscous results in the first figure which show much better agreement with experiments, underscoring the need for viscous simulations.

Since viscous simulations are more expensive, a strategy for populating a database of solutions for use in risk assessment is to use mostly inviscid simulations and a few viscous simulations. The viscous results are then used to correct the inviscid axial force values. The corrected inviscid results can now be used to predict the behavior of the vehicle. After the corrected inviscid results are obtained, viscous simulation can be used to verify the results for critical conditions.

Finally, the axial force results as a function of Δx are presented for the purpose of determining the probability of recontact in Fig. 11. During the abort, a recontact can be observed between the capsule and the SM if the proximity drag rise between Δx/d=0 and Δx/d=0.2 is too high for the escape motor thrust to overcome. The axial forces for this scenario are computed using both inviscid and viscous simulation for two different thrust levels of the escape motor. The different thrust levels correspond to the nominal thrust case and the low thrust case (due to low propellent grain temperature). The results show that there is enough thrust in both cases to overcome the drag and the weight of the

LEV. If a drag correction is applied to the inviscid results for the low thrust case, the possibility of recontact is present because drag+weight exceeds the escape motor thrust during the drag peak.

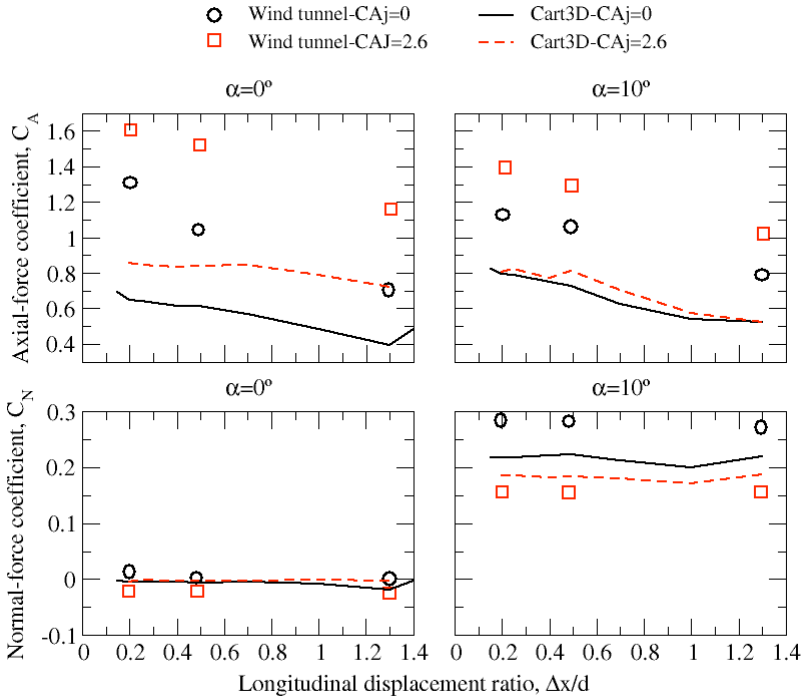


Figure 9b. Thrust and angle of attack effect on axial and normal-force coefficient with respect to Δx, *M=0.9,* Δz/d*=0,* $\Delta\alpha_s$*=10°*

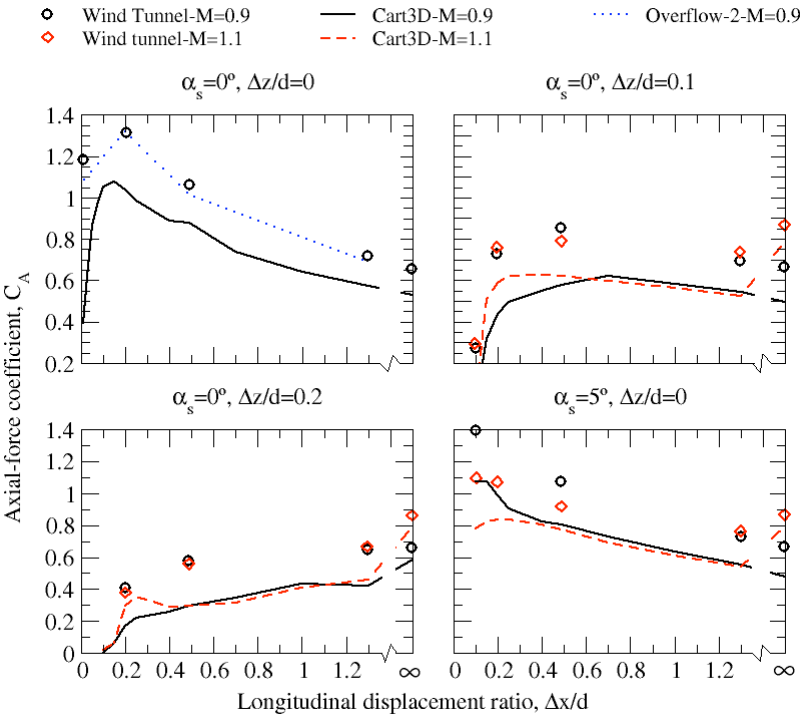


Figure 10a. Effect of Mach number and SM position on axial-force coefficient with respect to Δx, *CAj=0,* α*=0°,* ∞ *indicates no SM*

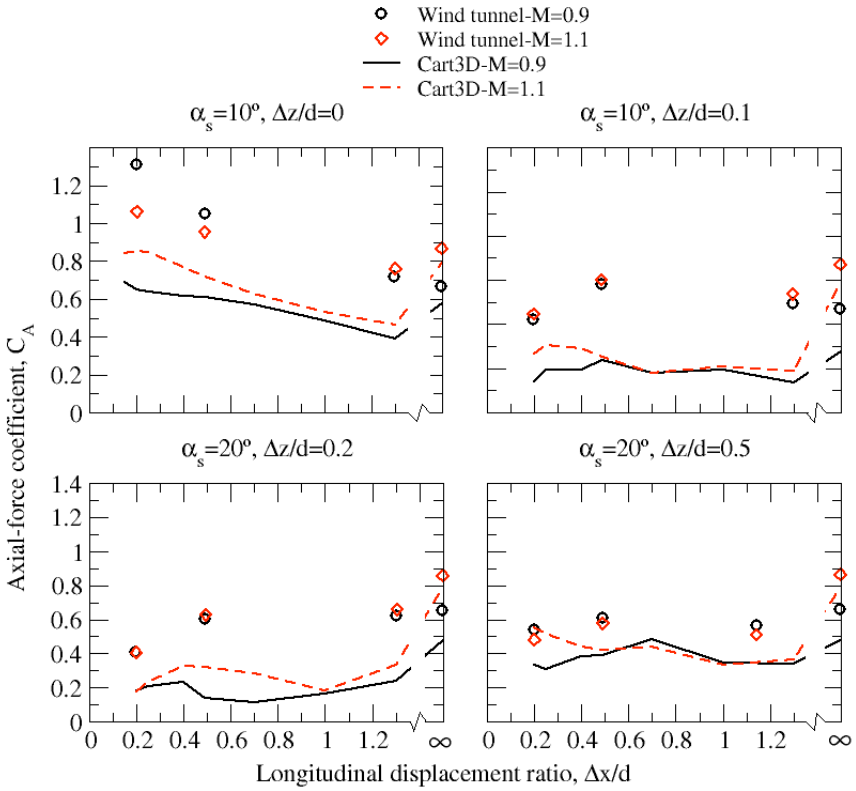


Figure 10b. Effect of Mach number and SM position on axial-force coefficient with respect to Δx, *CAj=0,* α*=0°,* ∞ *indicates no SM*

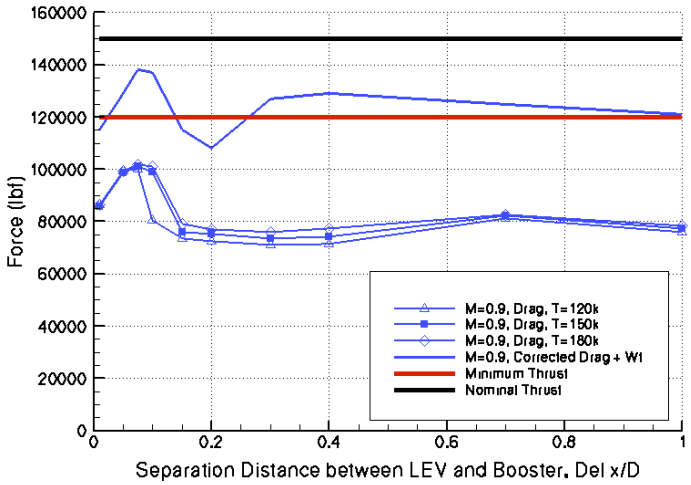


Figure 11. Axial force as a function of separation

V. Capsule/Booster separation

A time-dependent simulation of the separation of the LEV from the booster rocket is necessary to properly predict the potential recontact between the booster and the LEV. The need to avoid recontact for astronaut safety due to damage to the capsule can be a driving factor for the abort motor design. A time-dependent simulation of the abort

separation is performed with fluid flow as well as solid body dynamics models. The result is a time-dependent solution, which describes the forces and moments as a function of time as well as the resulting trajectories of the vehicles. In the present simulation we assume that the booster is moving at a constant speed after separation. The trajectory of the LEV with respect to the initial position at abort initiation is shown in Figure 12 for the nominal thrust value of 150000 pounds.

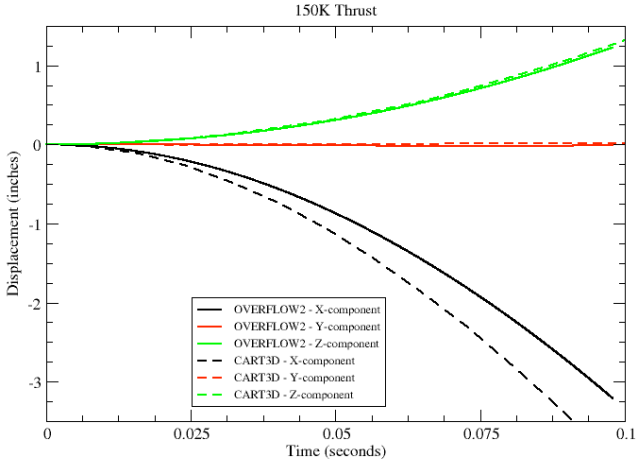


Figure 12. LEV trajectory from a dynamic simulation

At lower LEV thrust values, due to lower grain soak temperature, the 6-DOF inviscid simulation with a viscous correction exhibits recontact. Though the viscous correction is based on α=0° cases, the correction remain valid as the LEV does not develop a large angle of attack. Similarly, the 6-DOF viscous, time-dependent computation predicts recontact at the lower thrust level verifying the static aerodynamics prediction. The results of this lower thrust (120000 lbf) simulation are shown in Fig. 13. The initial condition is shown in Fig. 13a. The booster is represented by the service module and the capsule and escape system are mounted atop the SM. Figure 13a represents the moment at which the abort is initiated. The escape motor is fired and the dynamic simulation begins. Figure 13b shows a close up of the SM/capsule junction at the moment of recontact. Due to the insufficient thrust, no axial separation occured and the base of the heat shield impacts sideways into the lip of the SM.



Figure 13a. Navier-Stokes 6-DOF simulation of abort initiation (velocity magnitude)

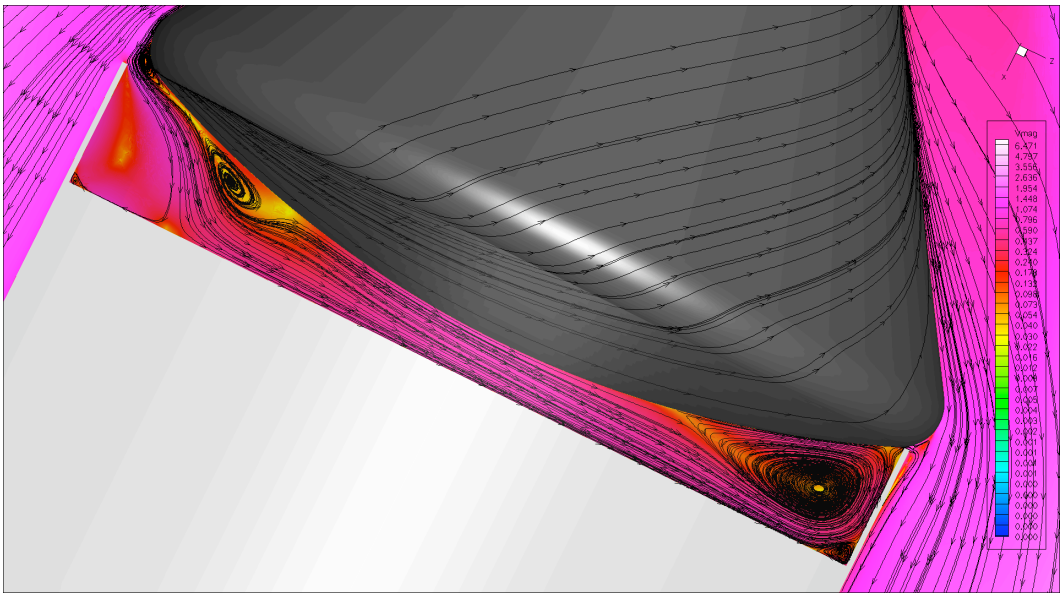


Figure 13b. Snapshot of the 6-DOF Navier-Stokes simulation at the moment of recontact (shown are velocity magnitude contours with instantaneous streamlines)

VI. Concluding remarks

The viscous simulation results agree well with the wind tunnel experiments. The inviscid results produce similar trends, but not the absolute levels of the axial force. However, viscous corrections to the inviscid results are possible and useful from the perspective of obtaining accurate predictions more efficiently.

These concepts are applied to investigate the possibility of recontact. The results show that the nominal thrust is enough to get the LEV away from the booster. However, if the grain temperature is below nominal values, lower resultant thrust is produced by the escape motor. This increases the probability of recontact.

A dynamic simulation with the time-accurate flow code running in tandem with a six-degrees of freedom dynamics module is employed to further verify the accuracy of the static analysis. Trajectories of viscous corrected inviscid results are found to closely match the viscous results.

Acknowledgments

The authors thank the members of the SARA project at NASA Ames Research Center for their support.

References

1. J. F. McCarthy Jr., J. Ian Dodds, and R. S. Crowder, “Development of the Apollo launch escape system”, J. Spacecraft, Vol. 5, No. 8, Aug. 1968, pp. 927-932.
2. D. L. Babcock, and P. D. Wiltse, “Motor-vehicle interfaces in the Apollo launch escape system”, AIAA Paper No. 65-152.
3. Boeing, “Saturn V AS-507 launch vehicle operational abort and malfunctioned flight analysis”, NASA CR-130857, Jul. 1969.
4. Bobby L. Berrier, and Odis C. Pendergraft Jr., “Transonic aerodynamic characteristics of a powered wind-tunnel model of the Apollo launch escape vehicle during separation”, NASA TM-X-1336.
5. William C. Mosley Jr., and Joseph C. Martino, “Apollo wind-tunnel testing program – historical development of general configurations”, NASA TN-D-3748, Dec. 1966.
6. M. J. Aftosmis, M. J. Berger, and J. E. Melton, “Robust and efficient Cartesian mesh generation for component-based geometry”, AIAA paper no. 97-0196, Jan. 1997.
7. P. G. Buning, D. C. Jespersen, T. H. Pulliam, W. M. Chan, J. P. Slotnick, S. E. Krist, and K. J. Renze, “OVERFLOW user’s manual”, NASA.
8. W. M. Chan, “The OVERGRID interface for computational simulations on overset grids,” *AIAA Paper No. 2002-3188*, 2002.
9. William C. Mosley Jr., and Bass Redd, “Aerodynamics stability characteristics of the Apollo launch escape vehicle (LEV) with canard surfaces deployed”, NASA TN-D-4280, Dec. 1967.
10. “Aerodynamics data manual for project Apollo”, NASA CR-82907, Feb. 1966.

11. S. M. Murman, M. J. Aftosmis, and M. J. Berger, “Simulations of 6-dof motion with a Cartesian method”, AIAA paper no. 2003-1246.
12. S. M. Murman, W. M. Chan, M. J. Aftosmis, and R. L. Meakin, “An interface for specifying rigid body motion for CFD applications”, AIAA paper no. 2003-1237, Jan. 2003.
13. System operations branch, Johnson Space Center, “CSM/LM Spacecraft Operational Data Book”, NASA TM X-68968, Aug. 1969.
14. W. M. Chan, R. J. Gomez, S. E. Rogers, and P. G. Buning, “Best Practices in Overset Grid Generation”, AIAA paper 2002-3191, 32nd AIAA fluid dynamics conference, St. Louis, Missouri, June 2002.
15. Manned Spacecraft Center, “Post Launch Report for Apollo Mission A-001”, NASA TM-X-66755, May 1964.